Accurate numerical simulation of the far-field tsunami caused by the 2011 Tohoku earthquake, including the effects of Boussinesq dispersion, seawater density stratification, elastic loading, and gravitational potential change

Toshitaka Baba[1], Sebastien Allgeyer[2], Jakir Hossen[3], Phil R. Cummins[2], Hiroaki Tsushima[4], Kentaro Imai[5], Kei Yamashita[6], and Toshihiro Kato[7]

Corresponding author: Toshitaka Baba, Graduate School of Science and Technology, Tokushima University, 2-1 Minami-jyosanjima-cho, Tokushima 770-8506, JAPAN; E-mail: baba.toshi@tokushima-u.ac.jp

[1]Graduate School of Science and Technology, Tokushima University, Tokushima, JAPAN

[2]Reseach School of Earth Science, The Australian National University, ACT, AUSTRALIA

[3]Department of Mathematics and Natural Sciences, BRAC University, BANGLADESH

[4]Meteorological Research Institute, Japan Meteorological Agency, Tsukuba, JAPAN

[5]Research and Development Center for Earthquake and Tsunami, Japan Agency for Marine-Earth Science and Technology, Yokohama, JAPAN

[6]International Research Institute of Disaster Science, Tohoku University, Sendai, JAPAN

[7] NEC Corporation, Tokyo, JAPAN

To be submitted to OCEAN MODELING

Abstract

In this study, we considered the accurate calculation of far-field tsunami waveforms by using the shallow water equations and accounting for the effects of Boussinesq dispersion, seawater density stratification, elastic loading, and gravitational potential change in a finite difference scheme. By comparing numerical simulations that included and excluded each of these effects with the observed waveforms of the 2011 Tohoku tsunami, we found that all of these effects are significant and resolvable in the far field by the current generation of deep ocean-bottom pressure gauges. Our calculations using previously published, high-resolution models of the 2011 Tohoku tsunami source exhibited excellent agreement with the observed waveforms to a degree that has previously been possible only with near-field or regional observations. We suggest that the ability to model far-field tsunamis with high accuracy has important implications for tsunami source and hazard studies.

Highlights

Accurate far-field tsunami simulation with a finite difference scheme.

Consideration of Boussinesq dispersion and water density stratification.

Consideration of elastic loading and gravitational potential change.

Tsunami computation using a high-performance computer.

Keywords: <u>2011 Tohoku tsunami, Numerical simulation,</u> Boussinesq dispersion, Elastic loading, Gravitational potential change, Seawater density stratification~~, Tsunami~~

1. Introduction

Bottom pressure gauges in the Deep-ocean Assessment and Reporting of Tsunamis (DART, Bernard and Meining, 2011) network recorded tsunami waveforms across the Pacific Ocean during the 2010 tsunami at Maule, Chile (e.g., Yamazaki and Cheung, 2011) and the 2011 tsunami at Tohoku, Japan (e.g., Fujii et al., 2011). Previous studies that compared these observations with predictions based on tsunami modeling noted systematic differences between the observed and modeled waveforms in the far field (e.g., Simons et al., 2011; Grilli et al., 2013; Fujii and Satake, 2013; Bai et al., 2015). The depth-integrated wave models used in these studies predicted the earlier arrival of the tsunamis by up to 15 minutes compared with the observations. Tsai et al. (2013) and Watada (2013) showed that the discrepancies in the arrival time can be explained by considering the deformation of the solid Earth and seawater compressibility.

In addition to the discrepancies in the arrival time, Watada et al. (2014) first systematically determined that a depression phase often emerges in the observed far-field waves preceding the first elevated tsunami waves. They suggested that the initial depression phase can be modeled by considering the solid Earth deformation due to the additional tsunami load and they developed a tsunami calculation method, which uses a phase correction technique derived from the normal mode theory of tsunamis coupled to the solid Earth (e.g., Watada and Kanamori, 2010). Their method considers the effects of seawater compressibility and elastic loading, as well as the effects of gravitational potential change due to mass movement caused by elastic loading and the frequency dispersion of water waves, thereby greatly improving the predictive accuracy for far-field tsunamis. The phase correction method is applied in the frequency domain to waves calculated using linear shallow water (LSW) theory, so the amplitude spectrum of a dispersive wave packet is preserved. This method also assumes that the tsunami is a unidirectional propagating wave; thus, it cannot be applied to nonlinear tsunamis, inundation, or the latter parts of tsunami wave trains, which typically include multiple arrivals. However, the maximum amplitude of a tsunami often occurs in the later phases at the coast, especially in far-field tsunamis (Hayashi et al., 2012). From the perspective of tsunami disaster mitigation, it is important to accurately calculate the leading wave and later phases, as well as accounting for nonlinear effects and inundation.

Numerical simulations using the finite difference method (FDM) can handle all of the effects described above simultaneously. It might seem that a huge computational cost would be incurred performing such FDM simulations, but developments in computer technology have increased the performance of computers by almost 1000-fold over the last decade. For example, the Supercomputer K was the fastest computer in the world from June 2011 to June 2012 with a performance of 10 petaflops (Fujitsu, 2011), whereas 40 teraflops was achieved by the 1st generation Earth Simulator (Japan Agency for Marine-Earth Science and Technology, 2002), which was the world's fastest computer from June 2002 to November 2004.

Allgeyer and Cummins (2014) developed a method that includes elastic loading and seawater density stratification in the finite difference scheme to solve the two-dimensional nonlinear shallow water equations. Baba et al. (2015) developed a large-scale parallelized code called "JAGURS" to solve the two-dimensional nonlinear shallow water equations with Boussinesq terms, and they successfully simulated soliton fission waves during the 2011 Tohoku tsunami observed in the near field. However, at present, no FDM code can consider all of these effects together. Thus, in the present study, the modules developed by Allgeyer and Cummins (2014) were merged with the Boussinesq parallelized code, JAGURS, including the contribution due to the gravitational potential change. This will be more useful in the future when high performance computers are more accessible. Using this new code, we calculated the trans-Pacific tsunami caused by the 2011 Tohoku, Japan earthquake and compared the results with the data observed at DART stations across the Pacific Ocean and costal tide gauges along the coast of Chile. We discuss the importance of considering these effects for making precise tsunami predictions.

2. Tsunami Simulation Model

2.1 Shallow water model with elastic loading and seawater density stratification

We begin by revisiting the method proposed by Allgeyer and Cummins (2014). A tsunami can be calculated by solving Euler's equation of motion and the equation of continuity. When applying Euler's equation of motion to a tsunami, we can consider the horizontal scale of water flow as much longer than the water depth. For large tsunamis, the dimension of the earthquake source is several tens to hundreds of km compared with an ocean depth of about 5 km, so the shallow water approximation is appropriate. Thus, we can consider that the vertical acceleration of water is much smaller than gravitational acceleration, and thus it is negligible. Therefore, the whole water mass from the bottom to the surface moves uniformly in the horizontal direction. In addition, by applying a boundary condition that the pressure is equal to the atmospheric pressure at the water surface, we can obtain the equation of motion in a two-dimensional spherical coordinate system,

$$\frac{\partial M}{\partial t}+\frac{1}{Rsin\theta}\frac{\partial}{\partial\varphi}\left(\frac{M^2}{H+\eta}\right)+\frac{1}{R}\frac{\partial}{\partial\theta}\left(\frac{MN}{H+\eta}\right)$$

$$=-\frac{g(H+\eta)}{Rsin\theta}\frac{\partial\eta}{\partial\varphi}-fN-\frac{gn^2}{(H+\eta)^{7/3}}M\sqrt{M^2+N^2} \qquad (1)$$

$$\frac{\partial N}{\partial t}+\frac{1}{Rsin\theta}\frac{\partial}{\partial\varphi}\left(\frac{MN}{H+\eta}\right)+\frac{1}{R}\frac{\partial}{\partial\theta}\left(\frac{N^2}{H+\eta}\right)$$

$$=-\frac{g(H+\eta)}{R}\frac{\partial\eta}{\partial\theta}+fM-\frac{gn^2}{(H+\eta)^{7/3}}N\sqrt{M^2+N^2}\,, \qquad (2)$$

where *M* and *N* are the depth-integrated flow quantities equal to $(H+\eta)u$ and $(H+\eta)v$, respectively, along the φ (longitude) and θ (co-latitude) directions. The variables *u* and *v* are the water velocity, *H* is the depth of the ocean at rest, *R* is the Earth's radius, *t* is time, η is the difference in sea level at time *t* from its value at rest, and *g* is the gravitational acceleration. The second and third terms on the right-hand side are the Coriolis and bottom friction forces, respectively, where *f* is the Coriolis parameter and *n* is Manning's roughness coefficient. The volume change per unit time must be equal to the flow rate of water into the volume, so η, *M*, and *N* must satisfy the equation of continuity, as follows.

$$\frac{\partial\eta}{\partial t}=-\frac{1}{Rsin\theta}\left[\left(\frac{\partial M}{\partial\varphi}+\frac{\partial(Nsin\theta)}{\partial\theta}\right)\right] \qquad (3)$$

Equations (1), (2), and (3) are called the nonlinear shallow water equations, and they are used for tsunami numerical modeling, where they are often solved via the FDM (e.g., Satake, 1995).

Allgeyer and Cummins (2014) followed Hendershott (1972) and Tsai et al. (2013) by considering the effects of elastic loading and seawater density stratification, respectively, to obtain

$$\rho_H \frac{\partial(\eta+\xi)}{\partial t} = -\frac{\rho_{ave}}{Rsin\theta}\left[\left(\frac{\partial M}{\partial\varphi} + \frac{\partial(Nsin\theta)}{\partial\theta}\right)\right], \qquad (4)$$

for the equation of continuity, where ξ is the displacement at the seafloor from its depth H when at rest, and ρ_H and ρ_{ave} are the sea water density at the seafloor and the average along the vertical profile, respectively. The displacement of the seafloor was calculated by superimposing a Green's function that describes the Earth's elastic response to a unit mass load concentrated at a point on its surface. The Green's function is expressed as a sum over spherical harmonics of the form:

$$\mathrm{G}(\mathbf{r}',\mathbf{r}) = \mathrm{G}(\alpha) = \frac{R}{M_e}\sum_{n=0}^{\infty} h'_n P_n(\cos\alpha) \qquad (5),$$

where $\mathbf{r}$ denotes any position on the Earth's surface, the point mass is located at $\mathbf{r}'$, P_n refers to the n-th Legendre polynomial, α is the angular distance between $\mathbf{r}'$ and $\mathbf{r}$, R is the Earth radius ($6.371 \times 10^6\ m$), M_e is the mass of the Earth ($5.9736 \times 10^{24}\ kg$), and h'_n is the loading Love number of angular order n. As shown by Hendershott (1972), the seafloor displacement term ξ in Equation (4) can be calculated by convolving the Green's function (Equation 5) with the change in ocean depth $\eta + \xi$.

Allgeyer and Cummins (2014) used the Green's function obtained by Pagiatakis (1990) for the PREM layered Earth model (Dziewonski and Anderson, 1981) and solved (1), (2) and (4) (but they neglected the bottom friction force in their deep-ocean tsunami simulations) for the trans-Pacific tsunamis from the 2010 Maule, Chile and 2011 Tohoku, Japan earthquakes with the FDM. This successfully improved the agreement between calculated and observed tsunami waveforms in the deep ocean.

2.2 Gravitational potential change

Watada et al. (2014) demonstrated the importance of gravitational potential change for the far-field tsunami phase velocity, as well as the elastic loading and seawater compressibility. Together, the two effects of elastic loading and gravitational potential change are referred to as self-attraction and loading (SAL) effects in the field of physical oceanography. The variable oceanic mass (in this case, tsunami) loads the Earth and changes its gravity field via the processes of self-gravitation and crustal deformation. Allgeyer and Cummins (2014) did not include the gravitational potential change effect. The Green's function that they used for elastic loading (Equation 5) only gives the deformation of the seafloor due to a unit mass load concentrated at a point on its surface. Therefore, we incorporate the effect of gravitational potential change in the FDM calculation based on previous SAL studies (e.g., Hendershott 1972; Farrell and Clark, 1976; Ray, 1998; Stepanov and Hughes, 2004; Agnew 2007; Vinogradova et al., 2015). Vinogradova et al. (2015) showed that the vertical displacement of the seafloor relative to the geoid resulting from a unit mass load at angular distance α can be expressed in the form of a Green's function as

$$\mathrm{G}_{SAL}(\mathbf{r}',\mathbf{r}) = \mathrm{G}_{SAL}(\alpha) = \frac{-R}{M_e}\sum_{n=0}^{\infty}(1 + k'_n - h'_n)P_n(\cos\alpha) \qquad (6),$$

where k'_n and h'_n are the loading Love number of angular order n. We replace the Green's function in Equation (5) by that in Equation (6) in the present study.

2.3 Inclusion of a Boussinesq term

A tsunami is a gravity wave, so the short wavelength component of a tsunami is delayed relative to its long wavelength component, i.e., it exhibits frequency dispersion. The frequency dispersions of tsunamis have been recorded clearly by offshore tsunami observation networks. A Boussinesq-type approach that adds a dispersion term to the shallow water equations is often used to simulate dispersive tsunamis (e.g., Horillo et al., 2006; Løvholt et al., 2012; Kirby et al., 2013). The equations of motion for the nonlinear shallow water equations with Boussineq terms (Peregrine, 1972) are expressed as follows.

$$\begin{aligned}\frac{\partial M}{\partial t} + \frac{1}{Rsin\theta}\frac{\partial}{\partial\varphi}\left(\frac{M^2}{H+\eta}\right) + \frac{1}{R}\frac{\partial}{\partial\theta}\left(\frac{MN}{H+\eta}\right) \\ = -\frac{g(H+\eta)}{Rsin\theta}\frac{\partial h}{\partial\varphi} - fN - \frac{gn^2}{(H+\eta)^{7/3}}M\sqrt{M^2+N^2} \\ + \frac{H^2}{3Rsin\theta}\frac{\partial}{\partial\varphi}\left[\frac{1}{Rsin\theta}\left(\frac{\partial^2 M}{\partial\varphi\partial t} + \frac{\partial^2(Nsin\theta)}{\partial\theta\partial t}\right)\right] \qquad (7),\end{aligned}$$

$$\frac{\partial N}{\partial t}+\frac{1}{Rsin\theta}\frac{\partial}{\partial\varphi}\left(\frac{MN}{H+\eta}\right)+\frac{1}{R}\frac{\partial}{\partial\theta}\left(\frac{N^2}{H+\eta}\right)$$

$$=-\frac{g(H+\eta)}{R}\frac{\partial h}{\partial\theta}+fM-\frac{gn^2}{(H+\eta)^{7/3}}N\sqrt{M^2+N^2}$$

$$+\frac{H^2}{3R}\frac{\partial}{\partial\theta}\left[\frac{1}{Rsin\theta}\left(\frac{\partial^2 M}{\partial\varphi\partial t}+\frac{\partial^2(Nsin\theta)}{\partial\theta\partial t}\right)\right] \qquad (8).$$

The final terms on the right-hand sides of Equations (7) and (8) are the Boussinesq (dispersive) terms.

The Boussinesq numerical model requires a small mesh size to suppress numerical dispersion and it consumes much greater computer resources than the non-dispersive shallow water equations due to the implicit nature of the solution technique used to deal with dispersion terms. Baba et al. (2015) developed a high-speed code (JAGURS) that solves the nonlinear shallow water equations with Boussinesq terms, i.e., Equations (3), (7), and (8), with real bathymetry using parallel computers.

In the present study, we improved the JAGURS code (Baba et al., 2015) for far-field tsunami simulations. We replaced Equation (3) with Equation (4) to include the seawater density stratification and elastic loading effects using the method of Allgeyer and Cummins (2014), where the Green's function (Vinogradova et al., 2015) employed also considers the effect of gravitational potential change.

3. Numerical Scheme

The governing equations (Equations 4, 7, and 8) were solved by a FDM implementation using a staggered grid scheme. The integration over time was solved with a leapfrog method, so η was defined at time $t=l\Delta t$, and (M,N) were defined at $t = (l - 1/2)\Delta t$, where Δt is the time step and $l = 1,2,3 \ldots$ Except for the dispersion terms in Equations (7, 8), the terms were calculated explicitly from η^{l}, $M^{l-1/2}$, and $N^{l-1/2}$. Next, the dispersion terms containing time derivatives were solved using the iterative Gauss-Seidel method (Press et al., 1986) to obtain the flow quantities at the next step ($M^{l+1/2}, N^{l+1/2}$) (see the Appendix in Baba et al. (2015) for details of the FDM implementation). The method of Allgeyer and Cummins (2014) was used to include the elastic loading and seawater density stratification effects. The calculated values of $M^{l+1/2}, N^{l+1/2}$ were substituted into Equation (4) to obtain η^{l+1*} by assuming ξ^{l+1} is zero, where η^{l+1*} indicates the first approximation of the sea surface elevation at the time of $l+1$. The bottom deformation ξ^{l+1} was computed by the convolution of the mass distribution from the surface η^{l+1*} with the Green's function of the earth deformation loaded by a unit mass, including the effect of gravitational potential change. This convolution was computed in the wavenumber domain. At each time step, the elevation function (η^{l+1*}) was transformed into the wavenumber domain, the spectral multiplication was computed, and the product was transformed back into the spatial domain. The value of η^{l+1*} was corrected by the appropriate Equation (4) to give the final values of η^{l+1} . Next, $\eta^{l+1}, M^{l+1/2}$, and $N^{l+1/2}$, were used to solve the governing equations for the next step.

We employed a domain decomposition method in parallel computations. The data required to calculate the variables at the edges of the sub-domain were acquired from the adjoining sub-domain by message passing-interface routines. The convolution required to calculate the sea bottom deformation was solved by a parallelized Fast Fourier Transform library.

4. Calculation settings

We performed a simulation using the upgraded tsunami calculation code described above for the tsunami generated by the 2011 earthquake in Tohoku, Japan. We compared our calculated tsunami waveforms with those recorded by DART systems in the far-field and by tide gauges along the Chilean coast. For bathymetric data, we used the global 30 arc-second data provided by the General Bathymetric Chart of the Oceans (GEBCO), and used the same 30 arc-second grid spacing in the calculation. Tsunamis are affected strongly by coastal bathymetry, so accurate bathymetric data are needed to simulate tsunami waveforms for coastal tide gauge data. We also acquired the regional bathymetric data near Chile complied by the Hydrographic and Oceanographic Service of the Chilean Navy (SHOA, 2014, personal communication), which covers a region of 249E–303E and 60S–11S with a grid interval of 30 arc-seconds. The SHOA bathymetric data were merged with the GEBCO bathymetric data for the trans-Pacific Tohoku tsunami simulation. The region of calculation was set as a domain from 120E–300 E and 60S–60N to cover the Pacific Ocean. A single bathymetric grid was used in this study. The total numbers of the grid points were 21601 and 14401 along the longitude and latitude, respectively. A sponge buffer zone (Cerjan et al., 1985) was applied to the outer boundary to avoid the reflection of tsunami waves. The time step width was set as 0.5 seconds to satisfy the Courant–Friedrichs–Lewy stability condition. A uniform

Manning's coefficient of 0.025 s/m$^{1/3}$ was used for the whole computation region. The integral time was 28 hours to allow the tsunami to propagate across the whole Pacific Ocean. For the calculations, we used 256 nodes of the new Earth Simulator (the third generation, Japan Agency for Marine-Earth Science Technology, 2015) launched in June, 2015, which is a large-scale vector-type supercomputer comprising a total of 5120 NEC SX-ACE nodes, with total peak performance and memory of 1.3 petaflops and 320 TB, respectively.

Several rupture models are available for the 2011 Tohoku, Japan earthquake, e.g., by Ammon et al. (2011) based on seismic data inversion, Grilli et al. (2013) based on geodetic data inversion, Gusman et al. (2012) based on tsunami and GPS joint inversion, and Satake et al. (2013) based on tsunami inversion. These studies were interested in the rupture process of the 2011 Tohoku earthquake, but our study focused on how the tsunami propagated over long distances. In addition, Saito et al. (2011) and Hossen et al. (2015) ~~used~~ inverted tsunami waveform data to estimate the initial sea-surface displacement by assuming instant and time-dependent tsunami generation, respectively (Fig. 1). This approach has the advantage that no fault plane is assumed and it can account for tsunami generation that is not related to fault slip, such as submarine mass failure, which may have contributed to the generation of the tsunami during the 2011 Tohoku earthquake (Tappin et al., 2014). Therefore, we did not use earthquake rupture models in this study, but instead we used initial sea-surface displacement models as the initial source condition. Typically, LSW Green's functions have been used for tsunami inversion analysis (e.g., Baba et al., 2005; Fujii et al., 2011; Fujii and Satake 2013), but

Saito et al. (2011) and Hossen et al. (2015) used linear dispersive Green's functions instead to estimate the tsunami sources. We used the models of Saito et al. (2011) and Hossen et al. (2015) in our accurate far-field simulations because they were not biased by any assumption of fault slip and they also used a more accurate representation of the tsunami as a dispersive wave. The calculated tsunami waveforms were compared with the observational data recorded in the Pacific Ocean to evaluate the accuracy of the tsunami simulation. We also compared two calculated tsunami waveforms derived from the tsunami source models of Saito et al. (2011) and Hossen et al. (2014) in the sensitivity analysis.

We obtained bottom pressure data recorded by DART stations during the 2011 Tohoku tsunami to make comparisons with the observed data. We also downloaded the coastal tide gauge (pressure) data obtained at Constitución and Iquique, Chile, from the following website: www.ioc-sealevelmonitoring.org (Intergovernmental Oceanographic Commission, 2016). The theoretical tidal component was calculated using the Naotide software (Matsumoto et al., 2000) and removed from the observed data together with the absolute pressure value at rest. Some noise that was not related to the tsunami signal still remained, so we applied a Butterworth bandpass filter with a high cutoff frequency of 0.01 Hz and a low cutoff frequency of 0.0001 Hz by using the Seismic Analysis Code (Incorporated Research Institutions for Seismology, 2013). Figure 2 shows the locations of the DART buoys and coastal tide gauges used for the comparison performed in this study. We note that the same bandpass filter used with the DART and tide gauge data was applied to the calculated waveforms for the comparisons with the observed waveforms.

5. Results

Figure 3 compares the tsunami waveforms at DART21418, located relatively close to the 2011 Tohoku earthquake epicenter, DART51407 near Hawaii, and DART32401 near Chile. Black lines indicate the observed tsunamis. The calculated tsunami waveforms shown in red were derived from the source of Saito et al. (2011). Tsunami propagation was solved by the conventional LSW equations in Fig. 3a–c, with Boussinesq term (LBS) in Fig. 3d–f, by the nonlinear shallow water equations with Boussinesq term (NBS) in Fig. 3g–i, and by the nonlinear shallow water equations with Boussinesq term, effects of seawater density stratification, and elastic loading (NBS+SD+EL) in Fig. 3j–l. For Fig. 3m–o, we used the nonlinear shallow water equations with all effects considered, i.e., due to the Boussinesq term, seawater density stratification, elastic loading, and gravitational potential change (NBS+SD+EL+GP). The explicit equations used in each case are provided in Supplementary Information 1.

According to LSW modeling (Fig. 3a–c), the calculated tsunamis arrived earlier than the observations by about 1, 10, and 15 minutes at DART21481, 51407, and 32401, respectively. At DART21418, the calculated maximum amplitude of the tsunami was about 0.3 m larger than that of the observed waveform. A short-period wave that followed the first peak in the observed waveform was not apparent in the waveform simulated with the LSW modeling. In addition, the short-period energy in the simulated waveform at about 2 hours and later (shown by an arrow in Fig. 3d) was not evident in the observed waveform. For DART51407 and 32401, the short-period components were much more significant in the calculated waves than the observations, although the same band-pass filter was applied to both waveforms. The small sea surface depression (indicated by arrows in Figs 3b and 3c) preceding the first elevated wave recorded in the observations was not present in the calculated tsunami waveforms.

Saito et al. (2011) inverted the tsunami waveform recorded at DART21418 by using linear dispersive Green's functions to estimate the tsunami source. Therefore, it was expected that inclusion of the Boussinesq term (LBS, Fig. 3d) would yield better agreement between the observed and simulated tsunami waveforms at DART21418. However, the short-period component was still too large in the later part of the calculated tsunami waveforms. The Boussinesq term~~s~~ also had a strong influence by changing the shape of the tsunami waveforms at the stations near Hawaii (Fig. 3e, DART51407) and Chile (Fig. 3f, DART32401), which were not involved in the source analysis presented by Saito et al. (2011). The short period component in the calculated LBS tsunami waveforms was reduced compared with those obtained by LSW modeling (Figs 3b and 3c) and the LBS waveforms agreed better with the observed waveforms. However, the computed tsunami arrival times were still earlier than the observations. The small first depression in the observed tsunami waveforms was also not simulated by LBS modeling.

The effect of the nonlinear terms (NBS) can be seen in the comparison at DART21418. The agreement between the observed and calculated tsunami waveforms was noticeably improved in the later part of the waveform about 2 hours after the earthquake (arrows in Figs 3d and 3g).

According to the NBS+SD+EL model at DART21418 (Fig. 3j), the effects of seawater density stratification and elastic loading were small because of the short traveling distance. By contrast, at the DART51407 (Fig. 3k) and DART32401 (Fig. 3l), stations, the clear contributions of these effects in the modeled waveforms were evident in terms of the delay in the tsunami arrival time and a small depression phase preceding the first elevated wave, and thus the agreement between the simulated and observed tsunami waveforms was improved.

The agreement between the simulated and observed tsunami waveforms was improved further by including the gravitational potential change (NBS+SD+EL+GP) at DART51407 (Fig. 3n) and DART32401 (Fig. 3o), where the computed tsunami waveforms were delayed by a few minutes more than those computed without the effect of the gravitational potential change. The amplitude of the first depression phase increased, thereby agreeing better with the observations. However, there was no significant difference at DART21418 after including the effect of the gravitational potential change.

To investigate the sensitivity of the tsunami source models, we also calculated the tsunami waveforms generated from the time-dependent 2011 Tohoku tsunami source provided by Hossen et al. (2015), as shown in Fig. 4, where the tsunami was calculated using the nonlinear shallow water model with all other effects considered (NBS+SD+EL+GP). The tsunami waveforms obtained using the source of Hossen et al.

(2015) were basically similar to those produced using the source of Saito et al. (2011). However, detailed comparisons showed that the source of Hossen et al. (2015) provided better agreement with the tsunami arrival times at DART51407 near Hawaii and DART32401 near Chile (Fig. 4b and 4c). The tsunami arrival timing was delayed by a few minutes compared with that using the instant source model of Saito et al. (2011). This was expected because part of the tsunami generation occurred later than the earthquake origin time in the time-dependent model of Hossen et al. (2015) and as the propagation was mainly linear, this difference in tsunami generation timing was preserved in the tsunami arrival times at large distances. According to the model of Hossen et al. (2015) (Fig. 1), most of the sea-surface displacement occurred within an interval of 60–120 seconds after the initiation of the earthquake rupture, so this difference in timing is a subtle feature.

However, we were surprised to find that the observed waveform at DART21418 was actually fitted better by the instantaneous source of Saito et al. (2011) (Fig. 4a). We suggest that the short-wavelength component of the initial sea surface displacement in the model of Hossen et al. (2015) was too small to match the DART21418 waveform, but this short-wavelength component was much less apparent in the far-field waveforms due to dispersion.

The tsunami waveforms calculated from the sources of Saito et al. (2011) and Hossen et al. (2015) by solving the nonlinear shallow water equations with all effects considered are compared with those recorded by the other DART stations in Supplementary Information 2, and Figs S1, S2, and S3.

Next, the tsunami waveforms were calculated and compared with those observed at the coastal tide gauges in Chile. In Fig. 5, the waveforms shown in black are observations, whereas those in red and blue are those calculated from the source of Hossen et al. (2015) by using the linear and nonlinear shallow water equations, respectively, combined with all other effects. The noise is large relative to the tsunami signal because the coastal tide gauge records are affected by wind waves. The tsunami arrival was predicted slightly earlier than the observations, which was possibly due to the coarse grid spacing of 30 arc-seconds in the coastal bathymetric data used in this study because the tsunami arrival time was predicted well by the simulation at DART32401, located off the coast of Chile (Fig. 4c). A small depression phase preceding the first elevated wave was predicted by the simulation of the tide gauges along the Chile coast (Fig. 5). However, the amplitude was quite small relative to the noise level, so it was difficult to recognize in the coastal tsunami observation data. Differences between the linear and the nonlinear calculations can be seen in the phases that arrived later. The simulated maximum tsunami height was changed slightly due to the nonlinear effect.

6. Discussion

According to the comparisons in Figs. 3a–f, the Boussinesq term had a strong effect by changing the shape of the tsunami waveforms in both the near- (DART21418) and far-fields (DART51407, 32401). This was caused by the inherent dispersive effect where the short-wavelength energy propagated more slowly than the long-wavelength energy.

It is well known that nonlinear effects play an important role in the propagation of a tsunami into bays and harbors, whereas these effects are small in the deep ocean. However, nonlinear effects can be recognized by comparing the observed and simulated tsunami waveforms shown in Fig. 3d and 3g, possibly because the waves in the later parts of the waveforms were reflected waves from the Japanese coast, where the nonlinear effects were significant.

We found that the inclusion of elastic loading and seawater density stratification delayed the tsunami arrival time and the emergence of a small sea level depression preceding the first elevated wave (Figs. 3j–l). These effects increased with the tsunami travel distance, as noted by Allgeyer and Cummins (2014). After applying a modification to the gravitational potential change in Green's function for elastic loading (Figs. 3m–3o), the computed tsunamis agreed better with the observed tsunami waveforms at the stations near Hawaii and Chile.

These separate conclusions were mentioned in previous studies. Thus, Kirby et al. (2013) performed a sensitivity analysis of the frequency dispersion using the far-field tsunami waveforms recorded during the 2011 Tohoku tsunami. Saito et al. (2014) noted the importance of the nonlinear terms in the dispersive simulation of reflected tsunami waveforms. Watada et al. (2014) developed a phase correction method and stated the importance of tsunami dispersion in delaying short period energy with respect to long period waves, and in delaying very long period energy due to seawater compressibility, elastic loading, and the gravitational potential change. In this study, we combined all the effects of reflection and refraction on the actual bathymetry, nonlinearity, frequency dispersion, seawater density stratification, elastic loading, and gravitational potential change using a single FDM code, and demonstrated its high accuracy in a simulation of the 2011 Tohoku tsunami.

In addition to the high-performance simulation code, our detailed comparisons of the observed and modeled tsunami waveforms were facilitated by the existence of previously published, high resolution source models for the 2011 Tohoku tsunami (Saito et al., 2011; Hossen et al., 2015). These models are based on an extensive network of offshore sea-level observation systems, which recorded the tsunami in the near field. As discussed above (see Fig. 5), coastal tide gauge waveforms are difficult to model accurately because they are sensitive to shallow bathymetry data, which are often poor quality and low resolution. In addition, far-field tsunami waveforms have previously been difficult to model because of the effects considered in the present study. Thus, the ability to accurately model far-field tsunami waveforms should facilitate the use of far-field tsunami data and improve our understanding of the many tsunami sources that lack near-field data (Yoshimoto et al., 2016). It will also be important to examine whether time-dependent features of a tsunami source can be retrieved from the far-field tsunami waveforms alone.

The source models of Hossen et al. (2015) and Saito et al. (2011) provide excellent fits to the deep-ocean DART data obtained off Chile. Therefore, we may confidently attribute the inadequate fit between the modeled and observed waveforms obtained from tide gauges along the Chilean coast to the limited resolution of the near shore bathymetry data. In a future study, we will attempt to model the 2010 Maule, Chile tsunami by simulating tide gauge records obtained on the Japan coast, where high-precision and high-resolution bathymetric data are available, in order to determine how accurately we can predict the far-field tsunamis at the coast.

Our method accurately simulated the far-field tsunami waveforms (Figs 3, S2, and S3), but further improvements can be made. We assumed that the Earth is perfectly spherical and that the gravitational acceleration is constant everywhere on the Earth in the FDM calculation. The non-spherical shape of the Earth will change the distance calculation over its surface and the gravity value at each location differs slightly from that at others. According to Watada et al. (2014), these two effects will change the tsunami travel time by a few minutes. The method we used for correcting seawater density stratification (Tsai et al., 2013) is mathematically equivalent to applying a frequency-independent water depth correction. This correction is actually frequency-dependent (Watada et al., 2014) so our method may over-correct for short wavelengths. The shallow water equations with Boussinesq terms (Peregrine, 1972) are also an approximate model of dispersive water waves. It would be interesting to investigate how our results compare with those obtained using more advanced Boussinesq-type equations (e.g., Lynett et al., 2012; Kirby et al., 2013), as well as considering the effects of seawater density stratification, elastic loading, and gravitational potential change. After we address these sources of error, we may consider other sources of error, including how variations in the ocean sound speed and temperature/salinity affect the density and compressibility of seawater to change the tsunami propagation speed. Thus, although advances in computer performance have allowed us to make important improvements in the accuracy of far-field tsunami calculations, we need to carefully select a numerical model depending on the output we want from the simulation (tsunami source, maximum tsunami height, and arrival time), and based on the balance between the efficiency of the simulation and the computational capacity.

7. Conclusion

In this study, we developed an improved FDM code for solving the nonlinear shallow water equations by including the effects of Boussinesq dispersion, seawater density stratification, elastic loading, and gravitational potential change. Large-scale, parallel computations were performed using a recently installed supercomputer called the Earth Simulator, and the results were compared with the tsunami waveforms generated by the 2011 Tohoku earthquake, which were observed by DART systems in the deep ocean and by coastal gauges. We simulated tsunami waveforms using the shallow water equations with and without considering nonlinearity, Boussinesq dispersion, seawater density stratification, elastic loading, and gravitational potential change. Our comparison of the results showed that the match between the observed and modeled waveforms improved progressively as each of these effects was included. In this modeling process, we also established that for large tsunamis, the sea level variations inferred from the current generation by ocean bottom pressure gauges were sufficiently accurate to resolve these effects, and thus it is necessary to consider all of them to model far-field tsunami waveforms at an accuracy commensurate with the measurement error.

The differences in waveforms modeled with and without the effects considered in this study may seem small in comparison to features such as the maximum tsunami height, but they are potentially important for studies of tsunami hazards. Indeed, during the 2006 and 2007 Kuril tsunamis, the maximum tsunami height observed on coastlines in the far field typically occurred hours after the arrival of the initial direct wave, where it was controlled by large-scale tsunami propagation, including multiple reflections from continental shelves and trans-ocean multipath propagation (Hayashi et al., 2012). In addition, recent large tsunamis such as the 2004 Indian Ocean tsunami, the 2010 Chile tsunami, and the 2011 Tohoku tsunamis resulted in far-field excitation with harbor resonance many hours after the passage of the primary tsunami, which were attributed to late-arriving, dispersed tsunami wave trains (Okal et al., 2006a, b; Wilson et al., 2013). The ability to accurately model far-field tsunami waveforms will facilitate the detailed study of these phenomena. Therefore, we consider that the results of this study will contribute to the mitigation of disasters caused by far-field tsunamis.

Availability

JAGURS source codes can be downloaded via GitHub (https://github.com/jagurs-admin/jagurs).

Acknowledgments

We thank Dr Tatsuhiko Saito for proving the digital data for the instantaneous tsunami source model of the 2011 Tohoku tsunami. We also thank Prof. Duncan Agnew and Dr

Shingo Watada for their suggestions to improve the model of elastic loading in the initial study (Allgeyer and Cummins, 2014). The regional bathymetric data obtained near Chile were provided by the Hydrographic and Oceanographic Service of the Chilean Navy (SHOA). The calculations in this study were performed using the Earth Simulator and we are grateful for being allowed access. We thank four anonymous reviewers and the editor, Dr William Perrie, whose constructive comments improved the manuscript. This study was partially supported by the Strategic Programs for Innovative Research, Field 3, and Australian Research Council grant DP120103207.

References

Agnew, D.C., 2007. 3.06 – Earth tides, Treatise on Geophysics, 3, 163–195, doi:10.1016/B978-044452748-6.00056-0.

Allgeyer, S., Cummins, P.R., 2014. Numerical tsunami simulation including elastic loading and seawater density stratification, Geophys. Res. Lett., 41, 2368–2375, doi:10.1002/2014GL059348.

Ammon, C.J., Lay, T., Kanamori, H., M. Cleveland, M., 2011. A rupture model of the 2011 off the Pacific coast of Tohoku earthquake, Earth Planets Space, 63, 693–696, doi:10.5047/eps.2011.05.015.

Baba, T., Cummins, P.R., Hori, T., 2005. Compound fault rupture during the 2004 off the Kii Peninsula earthquake (M7.4) inferred from highly resolved coseismic sea-surface deformation, Earth Planets Space, 57, 167–172.

Baba, T., Takahashi, N., Kaneda, Y., Ando, K., Matsuoka, D., Kato, T., 2015. Parallel implementation of dispersive tsunami wave modeling with a nesting algorithm for the 2011 Tohoku tsunami, Pure Appl. Geophys., 172, 3455–3472, doi:10.1007/s00024-015-1049-2.

Bai, Y., Cheung, K.F., Yamazaki, Y., 2015. Interconnection of multi-scale standing waves across the Pacific Basin from the 2011 Tohoku tsunami, Ocean Modell., 92, 183–197.

Bernard, E., Meinig, C., 2011. History and future of deep-ocean tsunami measurements, In Proceedings of Oceans' 11 MTS/IEEE, Kona, IEEE, Piscataway, NJ, 19–22 September 2011, No. 6106894, 7 pp.

Cerjan, C., Kosloff, D., Kosloff, R., Reshef, M., 1985. A nonreflecting boundary condition for discrete acoustic and elastic wave equations, Geophysics, 50, 705–708, doi:10.1190/1.1441945.

Dziewonski, A.M., Anderson, D. L., 1981. Preliminary reference Earth model, Physics of the Earth and Planetary Interiors 25 (4): 297–356, doi:10.1016/0031-9201(81)90046-7.

Farrell, W., and Clark, J., 1976. On postglacial sea level. Geophys. J. Int., 46, 647–667, doi:10.1111/j.1365-246X.1976.tb01252.x.

Fujii, Y., Satake, K., Sakai, S., Shinohara, M., Kanazawa T., 2011. Tsunami source of the 2011 off the Pacific coast of Tohoku Earthquake, Earth Planets Space, 63, 815–820.

Fujii, Y., Satake K., 2013, Slip distribution and seismic moment of the 2010 and 1960 Chilean earthquakes inferred from tsunami waveforms and coastal geodetic data, Pure Appl. Geophys., 170, 1493-1509, doi:10.1007/s00024-012-0524-2.

Fujitsu Corporation, 2011. press release, http://www.fujitsu.com/global/news/pr/archives/month/2011/20111102-02.html.

Grilli, S.T., Harris, J.C., Bakhsh, T.S.T., Masterlark, T.L., Kyriakopoulos, C., Kirby, J.T., Shi, F., 2013. Numerical simulation of the 2011 Tohoku tsunami based on a new transient FEM co-seismic source: Comparison to far- and near-field observations, Pure Appl. Geophys., 170(6-8), 1333–1359, doi:10.1007/s00024-012-0528-y.

Gusman, A.R., Tanioka, Y., Sakai, S., Tsushima, H., 2012. Source model of the great 2011 Tohoku earthquake estimated from tsunami waveforms and crustal deformation data, Earth Planet. Sci. Lett., 341, 234–242.

Hayashi, Y., Koshimura, S., Imamura, F., 2012. Comparison of decay features of the 2006 and 2007 Kuril Island earthquake tsunamis, Geophys. J. Int., 190, 347–357, doi: 10.1111/j.1365-246X.2012.05466.x.

Hendershott, M.C., 1972. The effects of solid Earth deformation on global ocean tides, Geophys. J. R. Astron. Soc., 29, 389–402,doi:10.1111/j.1365-246X.1972.tb06167.x.

Horillo, J., Kowalik, Z., Shigihara, Y., 2006. Wave dispersion study in the Indian Ocean-tsunami of December 26, 2004, Marine Geodesy, 29, 149–166.

Hossen, M.J., Cummins, P.R., J. Dettmer, J., Baba, T., 2015. Tsunami waveform inversion for sea surface displacement following the 2011 Tohoku earthquake:

Importance of dispersion and source kinematics, J. Geophys. Res. Solid Earth, 120, 6452–6473, doi:10.1002/2015JB011942.

Hydrographic and Oceanographic Service of the Chilean Navy (SHOA), 2014. Regional bathymetric charts around Chile, personal communication.

Incorporated Research Institutions for Seismology, 2013. Software downloads – SAC version 101.6a, http://ds.iris.edu/ds/nodes/dmc/software/downloads/sac/

Intergovernmental Oceanographic Commissions (January 15, 2016, final access date), Sea level station monitoring facility, http://www.ioc-sealevelmonitoring.org/.

Japan Agency for Marine-Earth Science and Technology, 2002. Earth Simulator: System Overview (ES) http://www.jamstec.go.jp/es/en/es1/system/performance.html.

Japan Agency for Marine-Earth Science and Technology, 2015. Earth Simulator, http://www.jamstec.go.jp/es/en/output/publication/brochures/es201510e.pdf.

Kirby, J.T., Shi, F., Tehranirad, B., Harris, J.C., Grill, S.T. 2013. Dispersive tsunami waves in the ocean: Model equations and sensitivity to dispersion and Coriolis effects, Ocean Modelling, 62, 39–55.

Løvholt, F., Kaiser, G., Glimsdal, S., Scheele, L., Harbitz, C.B., Pedersen, G., 2012. Modeling propagation and inundation of the 11 March 2011 Tohoku tsunami, Nat. Hazards Earth Syst. Sci., 12, 1017–1028, doi:10.5194/nhess-12-1017-2012.

Lynett, P., Borrero, J.C., Weiss, R., Son, S., Greer, D., Renteria, W. 2012. Observations and modeling of tsunami-induced currents in ports and harbors, Earth and Planet. Sci. Lett., 327–328, 68–74, doi:10.1016/j.epsl.2012.02.002.

Matsumoto, K., Takanezawa, T., Ooe M., 2000. Ocean tide models developed by assimilating TOPEX/POSEIDON altimeter data into hydrodynamical model: A global model and a regional model around Japan, J. Oceanogr., 56, 567–581.

National Oceanic and Atmospheric Administration, 2005. Deep-Ocean Assessment and Reporting of Tsunamis (DART(R)). National Geophysical Data Center, NOAA. doi:10.7289/V5F18WNS.

Okal, E.A., Fritz, H.M., Raad, P.E., Synolakis, C., Al-Shijbi, Y., Al-Saifi, M., 2006a. Oman Field Survey after the December 2004 Indian Ocean Tsunami. Earthquake Spectra, 22(S3):203–218.

Okal, E. A., Fritz, H. M., Raveloson, R., Joelson, G., Pancŏšková, P., Rambolamanana, G., 2006b. Madagascar Field Survey after the December 2004 Indian Ocean Tsunami. Earthquake Spectra, 22(S3):263–283.

Pagiatakis, S. D., 1990. The response of a realistic earth to ocean tide loading, Geophysical Journal International, 103(2), 541–560,doi:10.1111/j.1365-246X.

Peregrine, H., 1972. Equations for water waves and the approximations behind them, edited by R. E. Meyer, 95–121, Waves on Beaches and Resulting Sediment Transport, Academic Press, New York.

Press, W.H., Flannery, B.P., Teukolsky, S.A., Vetterling W.T., 1986. Numerical recipes, Cambridge Univ. Press, Cambridge.

Ray, R. D., 1998. Ocean self-attraction and loading in numerical tidal models, Marine Geodesy, 21, 181–192, doi:10.1080/01490419809388134.

Saito, T., Ito, Y., Inazu, D., Hino R., 2011. Tsunami source of the 2011 Tohoku-Oki earthquake, Japan: Inversion analysis based on dispersive tsunami simulations, Geophys. Res. Lett., 38, L00G19, doi:10.1029/2011GL049089.

Saito T., Inazu, D., Miyoshi, T., Hino, R., 2014. Dispersion and nonlinear effects in the 2011 Tohoku-Oki earthquake tsunami, J. Geophys. Res. Ocean, 119, 5160–5180, doi:10.1002/2014JC009971.

Satake, K., Fujii, Y., Harada, T., Namegaya, Y., 2013. Time and space distribution of coseismic slip of the 2011 Tohoku earthquake as inferred from tsunami waveform data, Bull. Seismol. Soc. Am., 103(2B), 1473–1492, doi:10.1785/0120120122.

Simons, M., et al., 2011. The 2011 magnitude 9.0 Tohoku–Oki earthquake: Mosaicking the megathrust from seconds to centuries, Science, 332, 1421–1425, doi:10.1126/science.1206731.

Stepanov, V. N., Hughes, C. W., 2004. Parameterization of ocean self-attraction and loading in numerical models of the ocean circulation. J. Geophys. Res., 109, C07004, doi:10.1029/2003JC002034.

Tappin, D.R., Grilli, S.T., Harris, J.C., Geller, R.J., Masterlark, T., Kirby, J.T., Shi, F., Ma, G., Thingbaijam, K., Mai, P.M., 2014. Did a submarine landslide contribute to the 2011 Tohoku tsunami? Mar. Geol., 357, 344–361.

Tsai, V.C., Ampuero, J.-P., Kanamori, H., Stevenson D.J., 2013. Estimating the effect of Earth elasticity and variable water density on tsunami speeds, Geophys. Res. Lett., 40, 492–496, doi:10.1002/grl.50147.

Vinogradova, N.T., Ponte, R.M., Quinn, K.J., Tamisiea, M.E., Campin, J.-M., Davis. J.L., 2015. Dynamic adjustment of the ocean circulation to self-attraction and loading effects, J. Phys. Oceano., 45, 678–689, doi:10.1175/JPO-D-14-0150.1.

Watada, S., Kanamori, H., 2010. Acoustic resonant oscillations between the atmosphere and the solid earth during the 1991 Mt. Pinatubo eruption, J. Geophys. Res., 115, B12319, doi:10.1029/2010JB007747.

Watada, S., 2013. Tsunami speed variations in density-stratified compressible global oceans, Geophys. Res. Lett., 40, 4001–4006, doi:10.1002/grl.50785.

Watada, S., Kusumoto, S., Satake K., 2014. Traveltime delay and initial phase reversal of distant tsunamis coupled with the self-gravitating elastic Earth, J. Geophys. Res. Solid Earth, 119, 4287–4310, doi:10.1002/2013JB010841.

Wilson, R.I., Admire, A.R., Borrero, J.C., Dengler, L.A., Legg, M.R., Lynett, P., Whitmore, P.M., 2013. Observations and impacts from the 2010 Chilean and 2011 Japanese tsunamis in California (USA). Pure and Applied Geophysics, 170(6–8), 1127–1147.

Yamazaki, Y., Cheung, K.F., 2011. Shelf resonance and impact of near-field tsunami generated by the 2010 Chile earthquake, Geophys. Res. Lett., 38, L12605, doi:10.1029/2011GL047508.

Yoshimoto, M, Watada, S., Fujii, Y., Satake, K., 2016. Source estimate and tsunami forecast from far-field deep-ocean tsunami waveforms – the 27 February 2010 Mw 8.8 Maule earthquake, Geophys. Res. Lett., 43, 659–665, doi:10.1002/2015GL067181.

Figure Captions

Fig. 1. Tsunami source models used in the calculations performed in this study. (a) Instantaneous tsunami generation (Saito et al., 2011) and (b–g) time-dependent tsunami generation (Hossen et al., 2015) models.

Fig. 2. The locations of the DART stations (triangles) and coastal tide gauges (circles) used in this study. The star indicates the epicenter of the 2011 Tohoku earthquake. Contours are the estimated tsunami arrival time in hours.

Fig. 3. Comparison of the observed (black) and simulated (red) tsunami waveforms at three DART stations. The simulations used the linear shallow water equations (LSW) for (a)–(c), the linear shallow water equations with the Boussinesq terms (LBS) for (d)–(f), the nonlinear shallow water equations with the Boussinesq terms (NBS) for (g)–(i), the nonlinear shallow water equations with the Boussinesq terms and the effects of sea water density stratification and elastic loading (NBS+SD+EL) for (j)–(l), and the nonlinear shallow water equations with the Boussinesq terms and the effects of sea water density stratification, elastic loading, and gravitational potential change for (m)–(o). The arrows in (b) and (c) indicate the small depression phase preceding the first elevated tsunami wave. The arrows in (d) and (g) are explained by the effect of the nonlinear terms in the Results section.

Fig. 4. Comparison of the different tsunami source models in Figure 1 at three DART stations. The black, red, and blue lines indicate the observation, simulations with the instantaneous source (Saito et al., 2011), and with the time-dependent source (Hossen et al., 2015), respectively. The nonlinear shallow water equations with Boussinesq terms and all the other effects of sea water density stratification, elastic loading, and gravitational potential change (NBS+SD+EL+GP) were used in the simulations.

Fig. 5. Comparison of the observations (black) and simulations at the coastal stations at Iquique and Constitución shown in Figure 1. Blue and red lines were derived from the linear and nonlinear shallow water equations, respectively, with Boussinesq terms and the effects of seawater density stratification, elastic loading, and gravitational potential changes. The time-dependent source (Hossen et al., 2015) was used as the tsunami's initial condition.

Supplementary Information - 1

Fig. 3 shows comparisons between the DART observations and our tsunami simulations. In order to clarify the contribution of each effect, the five cases were considered by changing the governing equations. We used a spherical coordinate system for simulations of a tsunami that travels a long distance over the Pacific Ocean. For Fig. 3a–c, the simulated tsunami waveforms were obtained with the conventional linear shallow water equations with Coriolis force as follows:

$$\frac{\partial M}{\partial t} = -\frac{gH}{Rsin\theta}\frac{\partial \eta}{\partial \varphi} - fN \qquad (S1)$$

$$\frac{\partial N}{\partial t} = -\frac{gH}{R}\frac{\partial \eta}{\partial \theta} + fM \qquad (S2)$$

$$\frac{\partial \eta}{\partial t} = -\frac{1}{Rsin\theta}\left[\left(\frac{\partial M}{\partial \varphi} + \frac{\partial (Nsin\theta)}{\partial \theta}\right)\right] \qquad (S3)$$

where *M* and *N* are the depth-integrated quantities equal to *Hu* and *Hv*, respectively, along longitude and latitude directions. The variables *u* and *v* are water velocity, and *H* is the depth of the ocean at rest, φ and θ are the longitude and co-latitude, respectively, *R* is the earth's radius, *t* is time, η is the sea surface elevation from the sea level at rest, *g* is the gravitational acceleration, *f* is Coriolis parameter. Equations (S1) and (S2) are the equations of motion. Equation (S3) is the equation of continuity.

The tsunami waveforms shown in Fig. 3d–f were obtained by solving the linear shallow water equations with Boussinesq terms. These tsunami waveforms were simulated with the Equation (S3) and the following equations of motion:

$$\frac{\partial M}{\partial t} = -\frac{gH}{Rsin\theta}\frac{\partial \eta}{\partial \varphi} - fN + \frac{H^2}{3Rsin\theta}\frac{\partial}{\partial \varphi}\left[\frac{1}{Rsin\theta}\left(\frac{\partial^2 M}{\partial \varphi \partial t} + \frac{\partial^2 (Nsin\theta)}{\partial \theta \partial t}\right)\right] \qquad (S4)$$

$$\frac{\partial N}{\partial t} = -\frac{gH}{R}\frac{\partial \eta}{\partial \theta} + fM + \frac{H^2}{3R}\frac{\partial}{\partial \theta}\left[\frac{1}{Rsin\theta}\left(\frac{\partial^2 M}{\partial \varphi \partial t} + \frac{\partial^2 (Nsin\theta)}{\partial \theta \partial t}\right)\right] \qquad (S5)$$

Furthermore, nonlinearity was considered for Fig. 3g–i in the equations of motion, that is,

$$\begin{aligned}
&\frac{\partial M}{\partial t} + \frac{1}{Rsin\theta}\frac{\partial}{\partial \varphi}\left(\frac{M^2}{H+\eta}\right) + \frac{1}{R}\frac{\partial}{\partial \theta}\left(\frac{MN}{H+\eta}\right) \\
&\qquad = -\frac{g(H+\eta)}{Rsin\theta}\frac{\partial h}{\partial \varphi} - fN - \frac{gn^2}{(H+\eta)^{7/3}} M\sqrt{M^2+N^2} \\
&\qquad + \frac{H^2}{3Rsin\theta}\frac{\partial}{\partial \varphi}\left[\frac{1}{Rsin\theta}\left(\frac{\partial^2 M}{\partial \varphi \partial t} + \frac{\partial^2 (Nsin\theta)}{\partial \theta \partial t}\right)\right] \qquad (S6),
\end{aligned}$$

$$\begin{aligned}
&\frac{\partial N}{\partial t} + \frac{1}{Rsin\theta}\frac{\partial}{\partial \varphi}\left(\frac{MN}{H+\eta}\right) + \frac{1}{R}\frac{\partial}{\partial \theta}\left(\frac{N^2}{H+\eta}\right) \\
&\qquad = -\frac{g(H+\eta)}{R}\frac{\partial h}{\partial \theta} + fM - \frac{gn^2}{(H+\eta)^{7/3}} N\sqrt{M^2+N^2} \\
&\qquad + \frac{H^2}{3R}\frac{\partial}{\partial \theta}\left[\frac{1}{Rsin\theta}\left(\frac{\partial^2 M}{\partial \varphi \partial t} + \frac{\partial^2 (Nsin\theta)}{\partial \theta \partial t}\right)\right] \qquad (S7).
\end{aligned}$$

For calculations of tsunami waveforms shown in Fig. 3j–l, we solved the nonlinear shallow water equations with Boussinesq terms, elastic loading and sea water density stratification effects considered. The equations of motion are the same as Equations (S6) and (S7). But the equation of continuity (S3) is replaced with the equation below,

$$\rho_H \frac{\partial (\eta + \xi)}{\partial t} = -\frac{\rho_{ave}}{Rsin\theta}\left[\left(\frac{\partial M}{\partial \varphi} + \frac{\partial (Nsin\theta)}{\partial \theta}\right)\right] \qquad (S8)$$

where ξ is the displacement at the seafloor from its depth H when at the rest. This was calculated by superimposing the Green's function (Equation (5) in the main text) that describes the Earth's response to a unit mass load concentrated at a point on its surface.

ρ_H and ρ_{ave} are sea water density at the seafloor and an average along the vertical profile, respectively.

For Fig. 3m–o, we used the same governing equations as above, Equations (S6), (S7), and (S8). But the different Green's function (Equation (6) in the main text) that includes the effect of gravitational potential change on its deformation was applied to calculate the displacement at the seafloor (ξ).

Supplementary Information - 2

We calculated far-field tsunami waveforms of the 2011 Tohoku tsunami by using the nonlinear shallow water equations with the effects of Boussinesq dispersion, seawater density stratification, elastic loading, and gravitational potential change included in our finite difference scheme. Fig. S1 shows the location of the DART buoys compared in the manuscript. We used the instant and the time-dependent tsunami sources of Saito et al. (2011) and Hossen et al. (2015) in Figs S2 and S3, respectively, for the initial sea-surface condition. Both results show excellent agreements between the observed and calculated waveforms.

Fig. S1. The locations of the DART stations are compared in Fig. S2 and S3. Star indicates the epicenter of the 2011 Tohoku earthquake. Contours are the estimated tsunami arrival time in hours.

Fig. S2. Comparison of tsunami waveforms between observation (black) and simulation (red) at the DART stations. We used Saito et al.'s (2011) tsunami source model for the tsunami propagation.

Fig. S3. Comparisons of tsunami waveforms between observation (black) and simulation (red) derived from Hossen et al.'s (2015) tsunami source model at the DART stations.

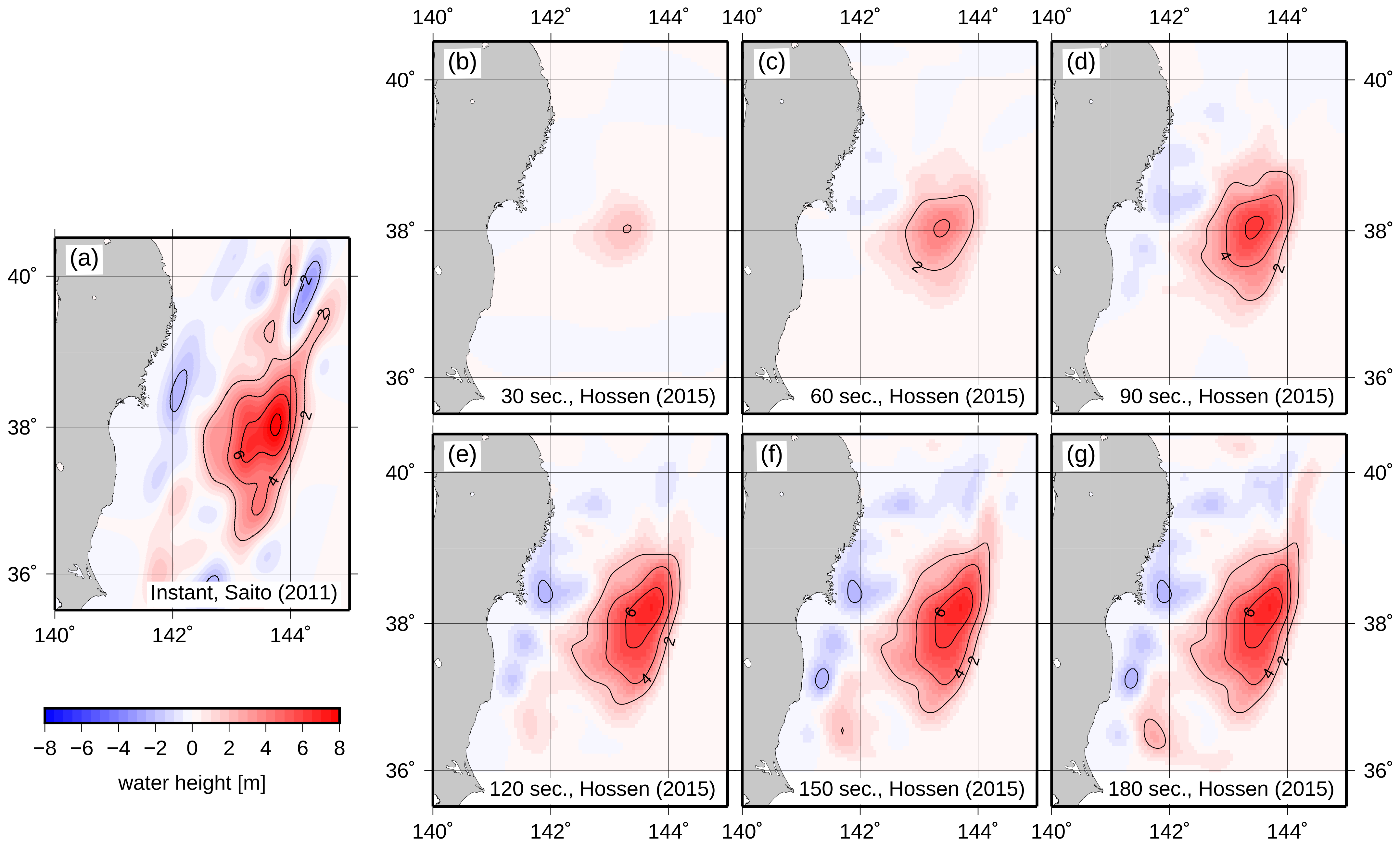

Fig.1, Baba et al.

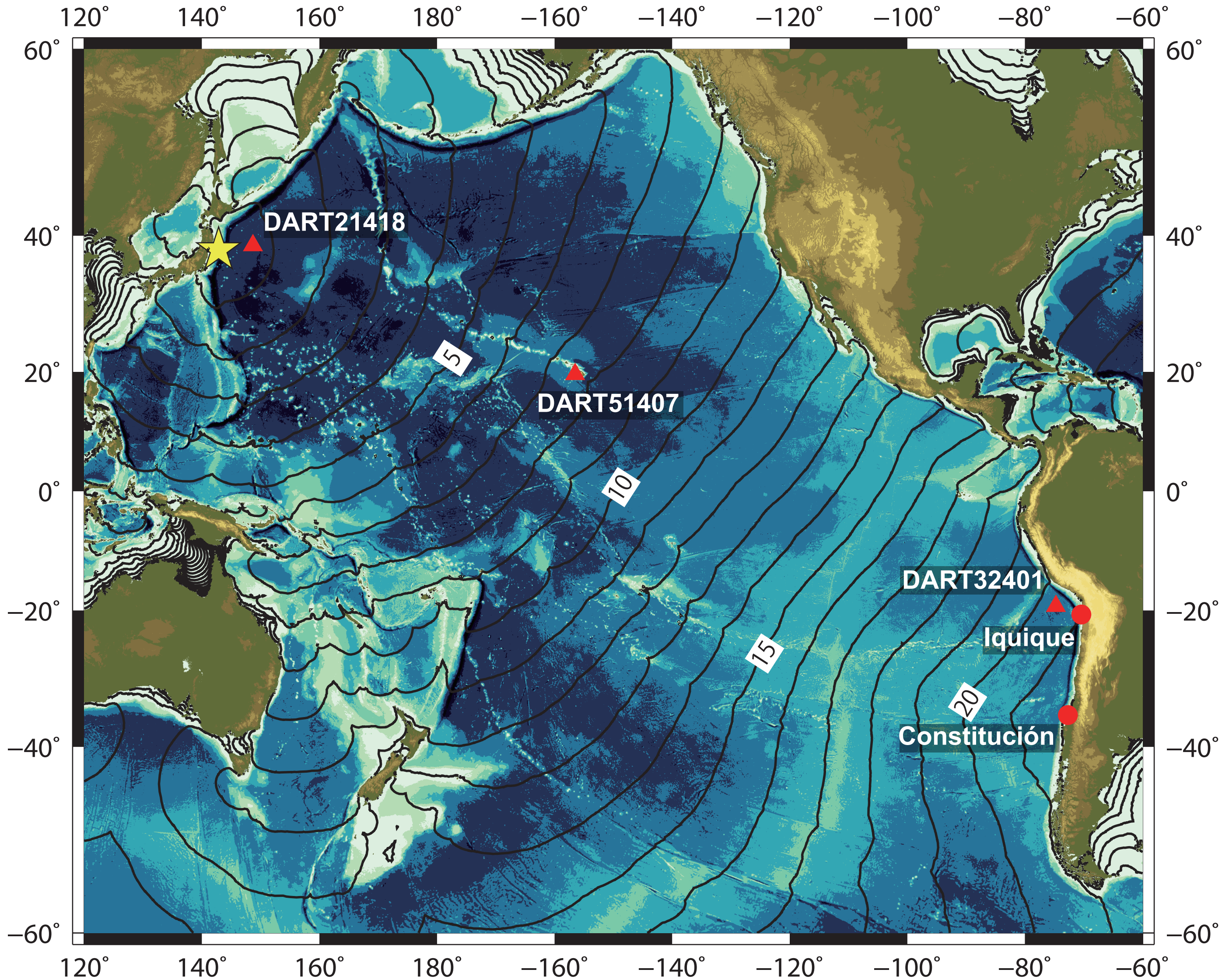

Fig.2 Baba et al.

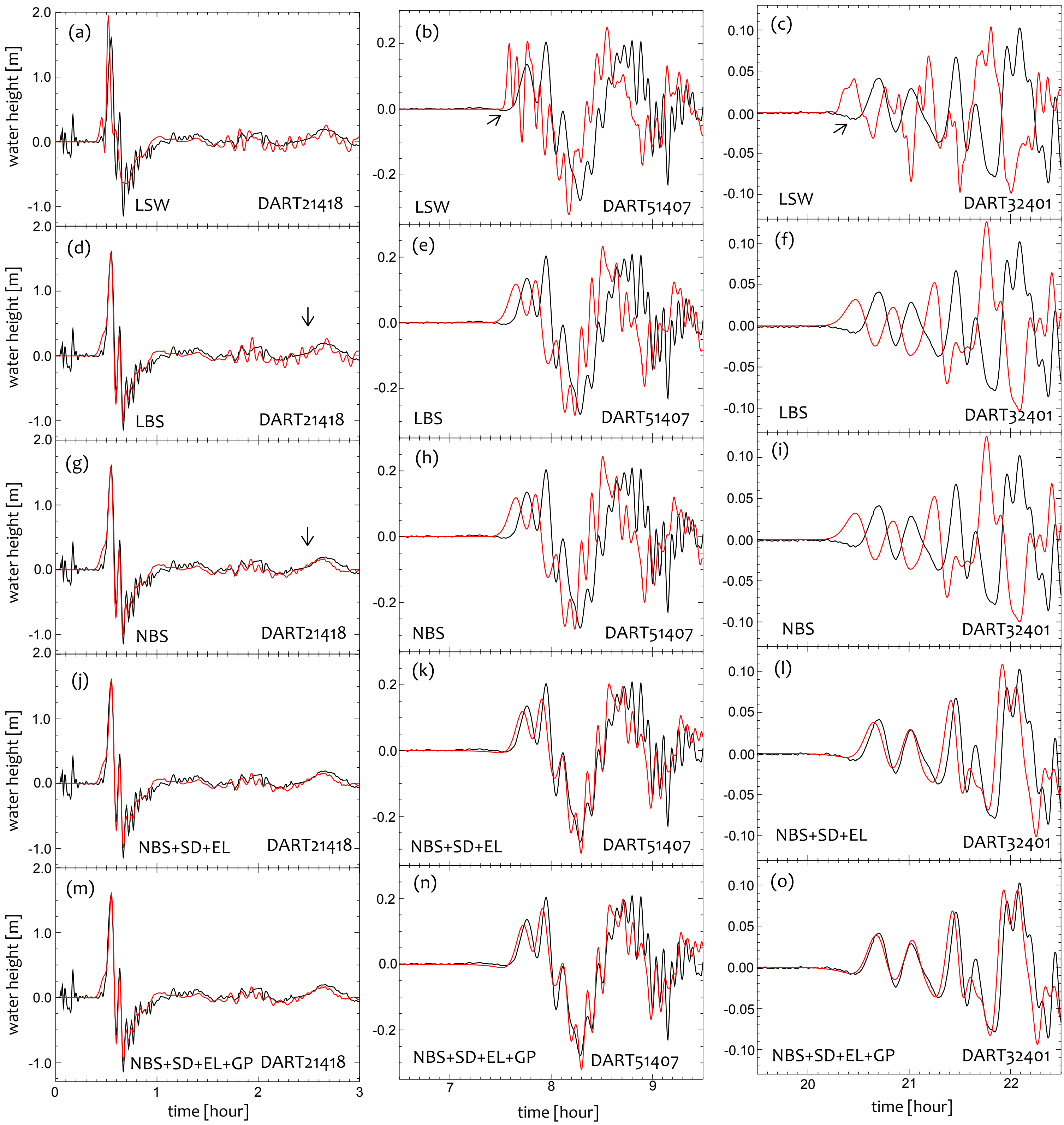

Fig.3 Baba et al.

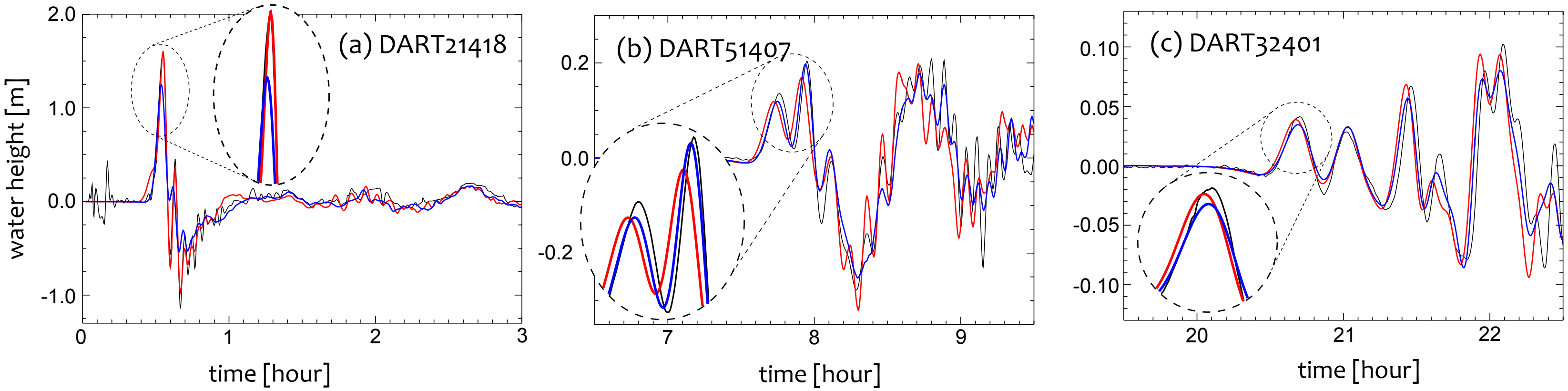

Fig.4 Baba et al.

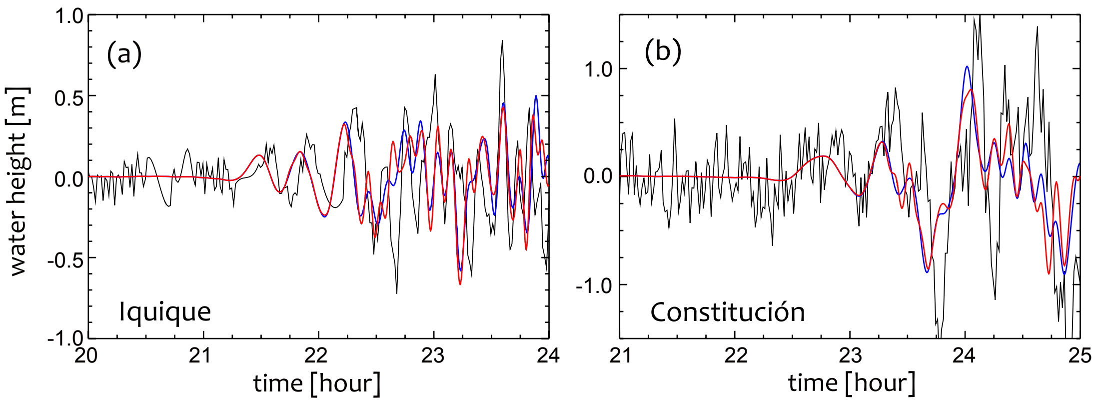

Fig.5 Baba et al.

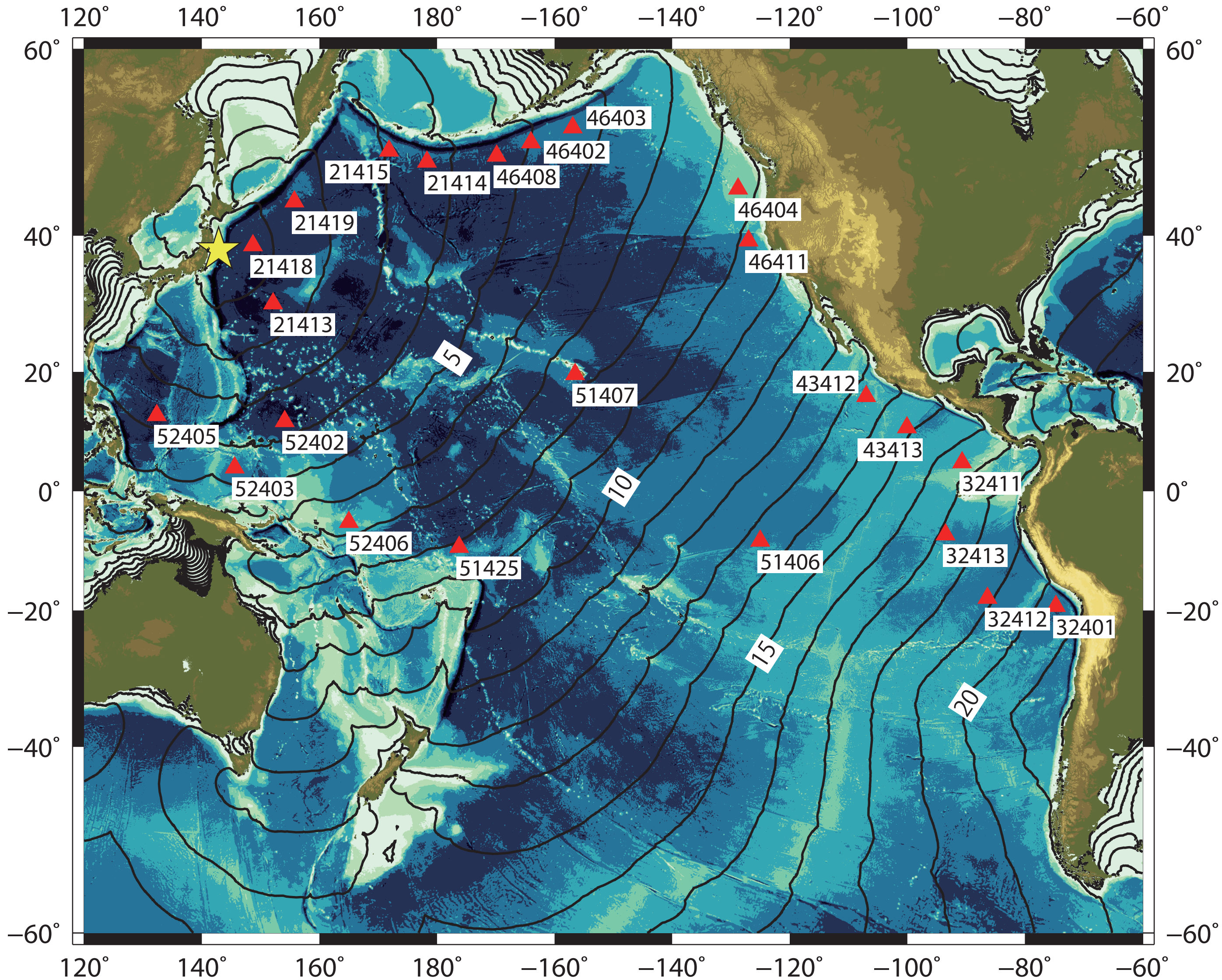

Fig. S1 Baba et al.

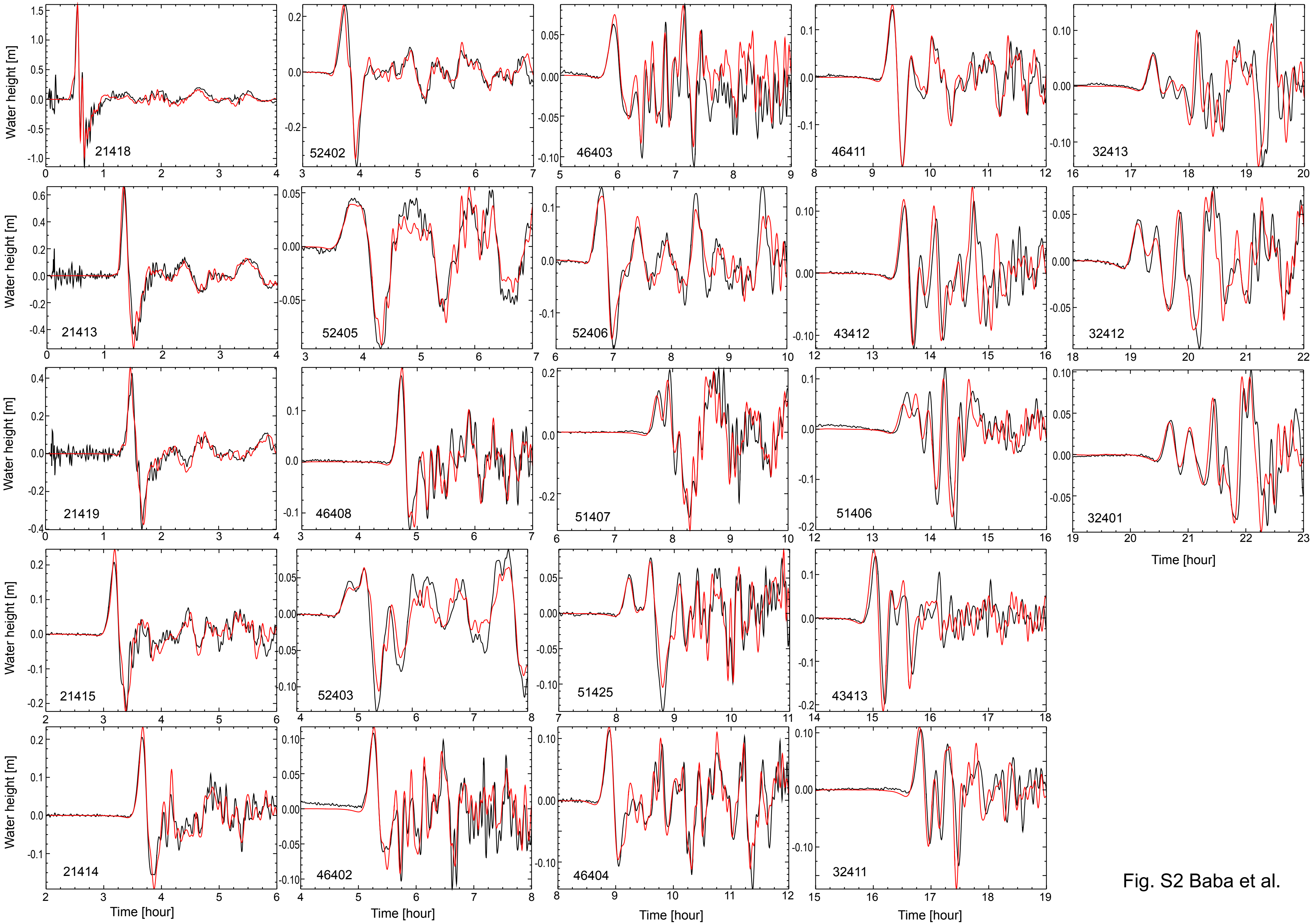

Fig. S2 Baba et al.

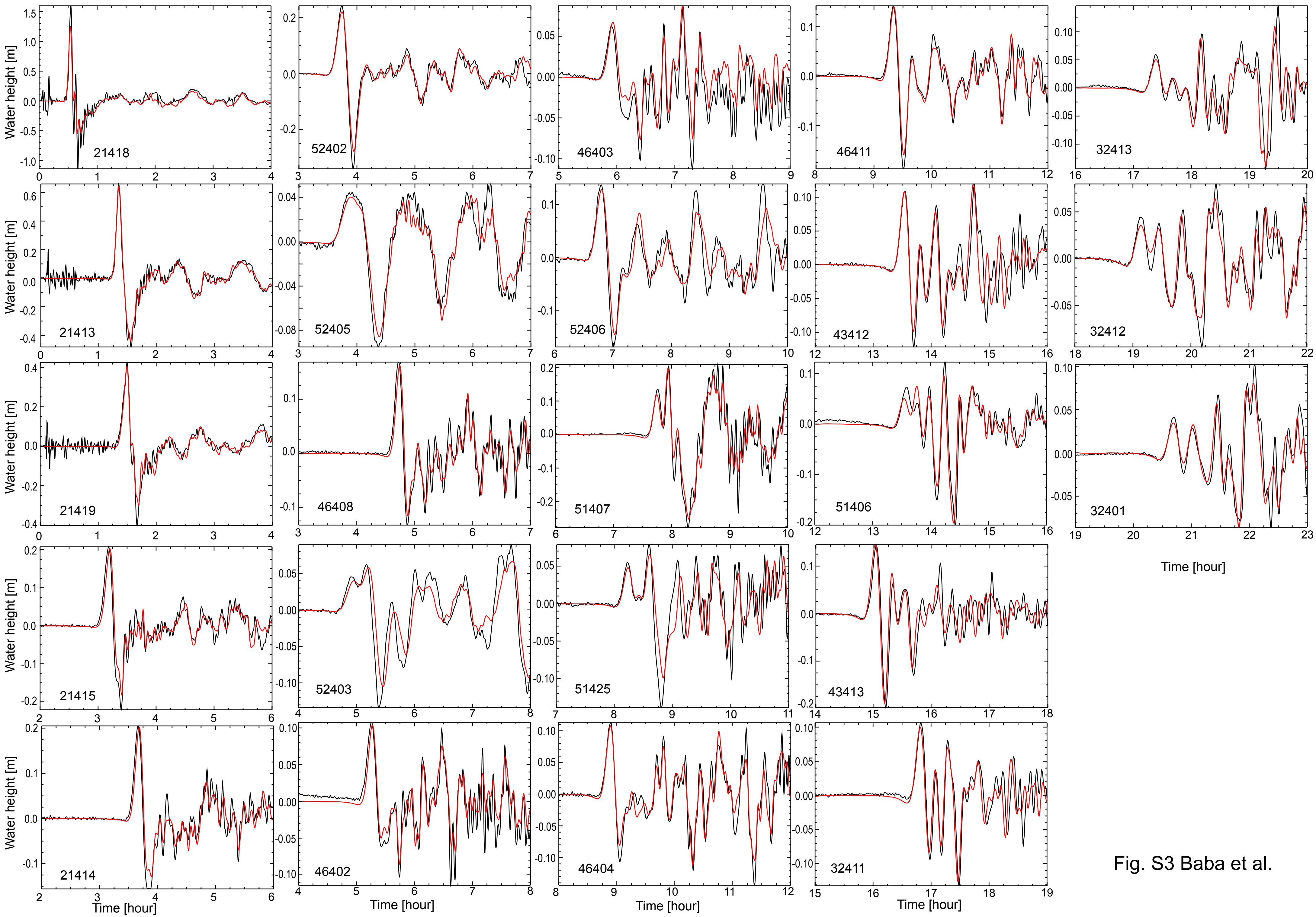

Fig. S3 Baba et al.